1484 *Biochemistry* **2007,** *46,* 1484−1494

Insight into the Radical Mechanism of Phycocyanobilin−Ferredoxin Oxidoreductase (PcyA) Revealed by X-ray Crystallography and Biochemical Measurements[†]

Shih-Long Tu,[‡,§] Nathan C. Rockwell,[§] J. Clark Lagarias,*,[§] and Andrew J. Fisher*,[§,||]

Institute of Plant and Microbial Biology, Academia Sinica, Nankang, Taipei 115, Taiwan, Section of Molecular and Cellular Biology, College of Biological Science, University of California, Davis, California 95616, and Department of Chemistry, University of California, Davis, California 95616

Received September 29, 2006; Revised Manuscript Received November 14, 2006

ABSTRACT: The X-ray crystal structure of the substrate-free form of phycocyanobilin (PCB)−ferredoxin oxidoreductase (PcyA; EC 1.3.7.5) from the cyanobacterium *Nostoc* sp. PCC7120 has been solved at 2.5 Å resolution. A comparative analysis of this structure with those recently reported for substrate-bound and substrate-free forms of PcyA from the cyanobacterium *Synechocystis* sp. PCC6803 (Hagiwara et al. (2006) *Proc. Natl. Acad. Sci. U.S.A. 103*, 27−32; Hagiwara et al. (2006) *FEBS Lett. 580*, 3823−3828) provides a compelling picture of substrate-induced changes in the PcyA enzyme and the chemical basis of PcyA's catalytic activity. On the basis of these structures and the biochemical analysis of site-directed mutants of *Nostoc* PcyA, including mutants reported in recent studies (Tu et al. (2006) *J. Biol. Chem. 281*, 3127−3136) as well as mutants described in this study, a revised mechanism for the PcyA-mediated four-electron reduction of biliverdin IXα to 3*E*/3*Z*-phycocyanobilin via enzyme-bound bilin radical intermediates is proposed. The mechanistic insight of these studies, along with homology modeling, have provided new insight into the catalytic mechanisms of other members of the ferredoxin-dependent bilin reductase family that are widespread in oxygenic photosynthetic organisms.

Phytobilins are heme-derived linear tetrapyrroles that function as chromophores for the light-sensing phytochrome photoreceptors and the light-harvesting phycobiliproteins of cyanobacteria, red algae, and cryptomonads (*1*). Light absorption by phytochromes effects the cis−trans isomerization of their bilin prosthetic groups, triggering a protein conformational change that initiates a signaling cascade responsible for altering many aspects of growth and development (*2*). In phycobiliproteins, by contrast, phytobilins function as antennae to absorb light energy and transfer it to photosynthetic reaction centers (*3*). Consequently, the biosynthesis of these linear tetrapyrroles is crucial for the environmental adaptation of oxygenic photosynthetic organisms.

The first committed intermediate of phytobilin biosynthesis is biliverdin IXα (BV[1]), a linear tetrapyrrole produced from heme by the oxygen-dependent enzyme heme oxygenase (*4*). In animals, BV is metabolized to bilirubin IXα (BR) by NADPH-dependent biliverdin reductases (*5*), but in plants and cyanobacteria, BV is metabolized by ferredoxin-dependent bilin reductases (FDBRs), a family of enzymes unique to oxygenic photosynthetic organisms (*6*). FDBRs utilize reduced ferredoxin as an electron donor to catalyze BV reduction, and different FDBRs possess distinct regiospecificities. Most FDBRs, including phytochromobilin (PΦB) synthase (HY2; EC 1.3.7.4), 15,16-dihydrobiliverdin (15,16-DHBV)−ferredoxin oxidoreductase (PebA; EC 1.3.7.2), and phycoerythrobilin (PEB)−ferredoxin oxidoreductase (PebB; EC 1.3.7.3), mediate two electron reductions, but phycocyanobilin (PCB)−ferredoxin oxidoreductase (PcyA; EC 1.3.7.5) catalyzes the four electron reduction of BV to yield PCB (*5*).

Our previous biochemical studies have established that BV reduction by PcyA proceeds via the two-electron reduced intermediate 18^1,18^2-DHBV, indicating that D-ring (exovinyl) reduction precedes A-ring (endovinyl) reduction (*6*). 18^1,18^2-DHBV is not released from the enzyme as a distinct product except under sub-optimal conditions. We have also shown that organic radical intermediates are produced during PcyA catalysis, as had been predicted on the basis of the apparent absence of any cofactors (*7*). More recently, chemical modification and site-directed mutagenesis studies demonstrated that a histidine−aspartate pair specific to PcyA were critical for the catalysis reaction (*8*). On the basis of these studies, we proposed a chemical mechanism involving a series of electron-coupled proton transfers utilizing reduced ferredoxin and the critical histidine−aspartate pair to mediate one-electron transfers concomitant with successive bilin protonations (*8*).

[†] This work was supported in part by USDA grant 2004-02962 to J.C.L., NSF grant MCB0515352 to A.J.F., and NSF grant PHY-0120999 to the Center for Biophotonics Science and Technology.

* Corresponding author. Phone: (530)-752-1865. Fax: 530-752-3085. E-mail: jclagarias@ucdavis.edu (J.C.L.). Phone: (530)-754-6180. Fax: 530-752-3085. E-mail: ajfisher@ucdavis.edu (A.J.F.).

[‡] Academia Sinica.

[§] Section of Molecular and Cellular Biology, University of California, Davis.

[||] Department of Chemistry, University of California, Davis.

[1] Abbreviations: ASU, crystallographic asymmetric unit; BR, bilirubin IXα; BV, biliverdin IXα; DHBV, dihydrobiliverdin; FDBR, ferredoxin-dependent bilin reductases; HY2, phytochromobilin synthase; NCS, non-crystallographic symmetry; NIR, near infrared; PCB, phycocyanobilin; PcyA, phycocyanobilin−ferredoxin oxidoreductase; PEB, phycoerythrobilin; PebA, 15,16-dihydrobiliverdin−ferredoxin oxidoreductase; PebB, phycoerythrobilin−ferredoxin oxidoreductase; PΦB, phytochromobilin; SeMet, selenomethionine.

10.1021/bi062038f CCC: $37.00

To evaluate this mechanistic proposal, we have undertaken the X-ray crystallographic analysis of PcyA from the filamentous cyanobacterium *Nostoc* sp. PCC7120, also known as *Anabaena* sp. PCC7120, and have used this information to guide further biochemical investigations. During the course of these studies, the crystal structures of substrate-bound and substrate-free forms of PcyA from *Synechocystis* sp. PCC6803 were reported (*9*, *10*). Here, we present the structure of substrate-free PcyA from *Nostoc* sp. PCC7120 with a focus on the mechanistic implications of the three crystal structures now available. Our analyses show that the overall folds of *Nostoc* and *Synechocystis* PcyAs are similar, revealing that significant conformational changes occur within the substrate-binding pocket upon BV binding. In particular, the critical histidine−aspartate pair previously characterized is repositioned upon substrate binding, suggesting that the imidazolium−carboxylate ion pair equilibrium shifts to favor a charge−neutral binding interaction with the BV substrate. Together with data on new site-directed mutants and additional biochemical analyses on the *Nostoc* enzyme, these studies have led to a revised mechanistic hypothesis for the four-electron reduction of BV to PCB by PcyA. Homology modeling of other FDBRs using these insights allows us to predict reaction mechanisms and identify potential catalytic residues of other FDBRs.

MATERIALS AND METHODS

Reagents. The chemical reagents used were those described previously unless otherwise specified (*8*). $18^1,18^2$-DHBV was prepared essentially as described previously (*6*). $18^1,18^2$-DHBV was first synthesized by acid scrambling and subsequent oxidation of a mixture of BRXIIIα and *meso*-BRIIIα. Products were extracted with the C18 SepPak cartridge (Waters, Milford, MA) and further separated with HPLC. Peak fractions of $18^1,18^2$-DHBV were collected, spectrophotometrically analyzed, vacuum-dried in measured aliquots, and stored at −20 °C in darkness prior to use. Bilin substrate concentrations were determined as described previously (*6*).

Site-Directed Mutagenesis, Expression, and Purification of Recombinant Nostoc PcyA. Site-directed mutagenesis of *Nostoc* PcyA was performed using the QuickChange Site-Directed Mutagenesis Kit (Stratagene) and plasmid pGEX-*pcyA* as the template (*8*). Mutant clones were characterized by DNA sequencing (Davis Sequencing). The expression and purification of wild-type and mutant recombinant *Nostoc* PcyA preparations were performed as described previously (*6*) with the following modifications. GST-free PcyA was purified by on-column cleavage overnight at 4 °C with PreScission protease (GE Healthcare Bio-Sciences, Piscataway, NJ) as recommended by the manufacturer. Cleaved PcyA was concentrated with Amicon Ultra 4-10,000 MWCO centrifugal filters (Millipore Corp, Billerica, MA) and further purified by Superdex G-200 (GE Healthcare Bio-Sciences, Piscataway, NJ) gel filtration chromatography in 20 mM Tris-HCl buffer at pH 8.0 containing 100 mM NaCl. Superdex G200-purified PcyA was dialyzed overnight against TS buffer (2 mM Tris-HCl buffer at pH 8.0 containing 10 mM NaCl) followed by concentration with Amicon centrifugal filters. Purified PcyA preparations were stored at −80 °C prior to analysis.

Crystallization of Nostoc PcyA. PcyA protein concentrations, determined by BCA assay (Pierce, Rockford, IL), were adjusted to 10 mg/mL with TS buffer. Primary screens were carried out for both substrate-bound and substrate-free PcyA by the sitting-drop method with Wizard screen I and II (Emerald BioSystems, Bainbridge Island, WA) at 293 K in the dark. The drop consisted of 1 μL of protein in TS buffer and 1 μL of precipitant solution. Several different drops resulted in needle-shaped crystals grown under comparable conditions (polyethylene glycol plus Ca^{2+}). Crystal growth optimization was performed using the hanging-drop method in 24-well Linbro plates with a drop size of 4 μL (2 μL protein/2 μL precipitant solution). Precipitating conditions for needle-shaped substrate-free crystals were expanded for optimization. Conditions were not found to produce BV-bound crystals that diffracted well. Conditions that resulted in the best diffracting substrate-free PcyA crystals was 18% PEG-8000, 0.025 M MES-NaOH at pH 6.5, 0.05 M $Ca(OAc)_2$ at pH 6.5, and 5% dioxane (or 5% ethanol).

Expression and Crystallization of Substrate-Free Selenomethionine-Labeled PcyA. For selenomethionine (SeMet) incorporation, PcyA was expressed in *E. coli* DH5α grown in M9 media. Fifteen minutes prior to the induction of PcyA expression with isopropyl thiogalactoside, a mixture of SeMet and other amino acids were added to inhibit amino acid synthesis as described (*11*, *12*). SeMet-labeled PcyA was purified and crystallized under the same conditions as unlabeled native PcyA, followed by multiwavelength anomalous diffraction (MAD) analysis.

Diffraction Data Collection and MAD Analysis of Nostoc PcyA. Individual needle-shaped PcyA crystals were sequentially transferred to 30% (v/v) ethylene glycol in mother liquor (cryo solution) and flash frozen in liquid nitrogen. X-ray diffraction data from native and SeMet crystals at 100 K were collected on beam lines 9-2 and 9-1, respectively, at the Stanford Synchrotron Radiation Laboratory (SSRL). Diffraction data were indexed and integrated with DENZO followed by reduction with SCALEPACK (*13*). Complete data sets were collected to 2.5 and 3.0 Å resolution for the native and SeMet PcyA crystals, respectively. Despite the fact that native and SeMet PcyA crystals were grown under similar conditions, native PcyA crystallized in space group $P2_1$, whereas the SeMet protein crystallized in space group $C2$ (Table 1). For native crystals, the Matthews coefficient V_M (*14*) was calculated to be 2.0 $Å^3$/Da, assuming 12 monomers per crystallographic asymmetric unit (ASU), which corresponds to a solvent content in the crystal of ∼38%. The SeMet crystals had three monomers per ASU ($V_M = 2.2$ $Å^3$/Da and a solvent content of ∼43%). The SeMet crystals were sensitive to radiation damage, resulting in poor diffraction after extended periods of X-ray exposure. This problem was compounded by the low symmetry of the $C2$ space group that required 360° of data collection for the high redundancy necessary for SeMet MAD structure determination. The SeMet structure was solved by collecting two diffraction data sets at the Se absorption peak and at a remote energy using the inverse beam method (Table 1). The two SeMet data sets were inputted into the program SOLVE (*15*), which was able to find 12 selenium sites in the asymmetric unit (overall figure of merit (FOM) was 0.45). The phases were improved by solvent flattening using the program RESOLVE (*16*, *17*), (FOM 0.70). Inspection of the solvent-

Table 1: Data Collection, Phasing, and Refinement Statistics

	Se peak	Se remote	native
SSRL beamline	BL 9-1	BL 9-1	BL 9-2
wavelength	0.97915 Å	0.89195 Å	0.9800 Å
resolution	3.00 (3.11 − 3.00) Å	3.00 (3.11 − 3.00) Å	2.50 (2.59 − 2.50) Å
space group		$C2$	$P2_1$
cell parameters	$a = 145.97$ $b = 73.06$ $c = 81.74$ $\beta = 122.75°$		$a = 78.50$ $b = 141.33$ $c = 121.84$ $\beta = 91.29°$
monomers/ASU		3	12
V_M (Å^3/Da); % solvent		2.2; 43%	2.0; 38%
no. of reflections	106,183	67,302	334,805
no. unique	14,793	14,513	91,664
R_{merge}^{a} (%)	7.9 (30.8)	9.3 (47.5)	8.4 (38.3)
mean $(I)/\sigma(I)$	21.6 (7.3)	98.2 (98.2)	13.9 (3.3)
completeness (%)	99.9 (99.9)	15.2 (3.5)	99.7 (100.0)
no. of Se sites	12		
figure of merit (SOLVE/RESOLVE)	0.45/0.70		
refinement statistics			
resolution (Å)			43.9−2.50
no. reflections ($F \geq 0$)			91,664
R-factor^b			21.1
R-free^b			25.8
rms bond length			0.016
rms bond angles			1.512
Ramachandran plot statistics			
residues^c			2,550
most favorable region (%)			93.7
allowed region (%)			6.1
generously allowed region (%)			0.1
disallowed (%)			0.0
asymmetric unit content			
nonhydrogen protein atoms			23,422
water			190
calcium ion			1

[a] Rmerge = $[\Sigma_h \Sigma_i |I_h - I_{hi}| / \Sigma_h \Sigma_i I_{hi}]$, where I_h is the mean of I_{hi} observations of reflection h. The numbers in parenthesis represent the highest resolution shell. [b] R-factor and $R_{free} = \Sigma||F_{obs}| - |F_{calc}||/\Sigma|F_{obs}| \times 100$ for 95% of recorded data (R-factor) or 5% of data (R_{free}). [c] The number of non-proline and non-glycine residues used for the calculation.

flatten electron density map clearly revealed a β-sheet sandwiched between some α-helices in which a partial model was built then rotated and translated into density that corresponded to the two other monomers in the asymmetric unit. The electron density was improved by molecular averaging using the program DM (*18*). The resultant average map was used to add most protein core side chains and some loops that connected the secondary structural elements. This more-complete 3.0 Å resolution SeMet model was used to solve the structure of native *Nostoc* PcyA using the 2.5 Å resolution data by molecular replacement using the program PHASER (*19*). PHASER was able to determine the positions of all 12 monomers in the $P2_1$ unit cell. Initial phases were calculated and improved by 12-fold NCS averaging, increasing the correlation coefficient from 0.615 to 0.870.

Nostoc PcyA Model Building and Structural Refinement. Model building was carried out with the molecular graphics program COOT (*20*). Maximum-likelihood coordinate and *B*-factor refinement were carried out with the program REFMAC (*21*) using 95% of the data to the respective maximum resolution. Tight noncrystallographic restraints were maintained for most of the protein core, and the loose restraints for the loop regions for the 12 monomers resulted in the lowest *R*-free value. The quality of the model was checked with the program PROCHECK (*22*, *23*), and the results are summarized in Table 1. The native apo PcyA atomic coordinates are deposited in the protein data bank, PDB accession number 2G18.

PcyA and HY2 Enzyme Assays. Recombinant *Nostoc* PcyA and *Arabidopsis thaliana* phytochromobilin synthase (HY2) were expressed and purified as described above and previously (*5*). Steady-state semi-aerobic and single-turnover anaerobic bilin reductase assays were performed as described previously (*7*, *8*). Absorption spectrophotometric measurements were obtained using a Hewlett-Packard HP8453 UV−Visible spectrophotometer. An Agilent Technologies Model 1100 Liquid Chromatograph was used for high performance liquid chromatography (HPLC) with a 4.6 × 250 mm Phenomenex Ultracarb 5-μm ODS (*20*) reverse phase column, an isocratic mobile phase consisting of 50% acetone and 50% 20 mM formic acid (by volume), and a flow rate of 0.6 mL/min (*6*).

Homology Modeling of Bilin Reductases. The 1.5 Å structure of PcyA with bound BV (*9*) was used as a template to generate apoprotein homology models with the program Modeller v8.0 (*24*) for HY2 from *A. thaliana* (residues 37−284) and PebA from *Synechococcus* sp. WH8020 (residues 1−236) from a sequence alignment of FDBRs (Figure S1, Supporting Information). These models were then superposed onto the PcyA holoprotein model in VMD (*25*), and coordinates for bound BV chromophore were transferred to the homology models. The resulting holoprotein models for HY2 and PebA were manually edited in VMD to lessen steric clash and then subjected to energy minimization in Gromacs 3.2.1 (*26*) using the parameters for BV derived from those reported for the structurally related chromophore PCB (*27*)

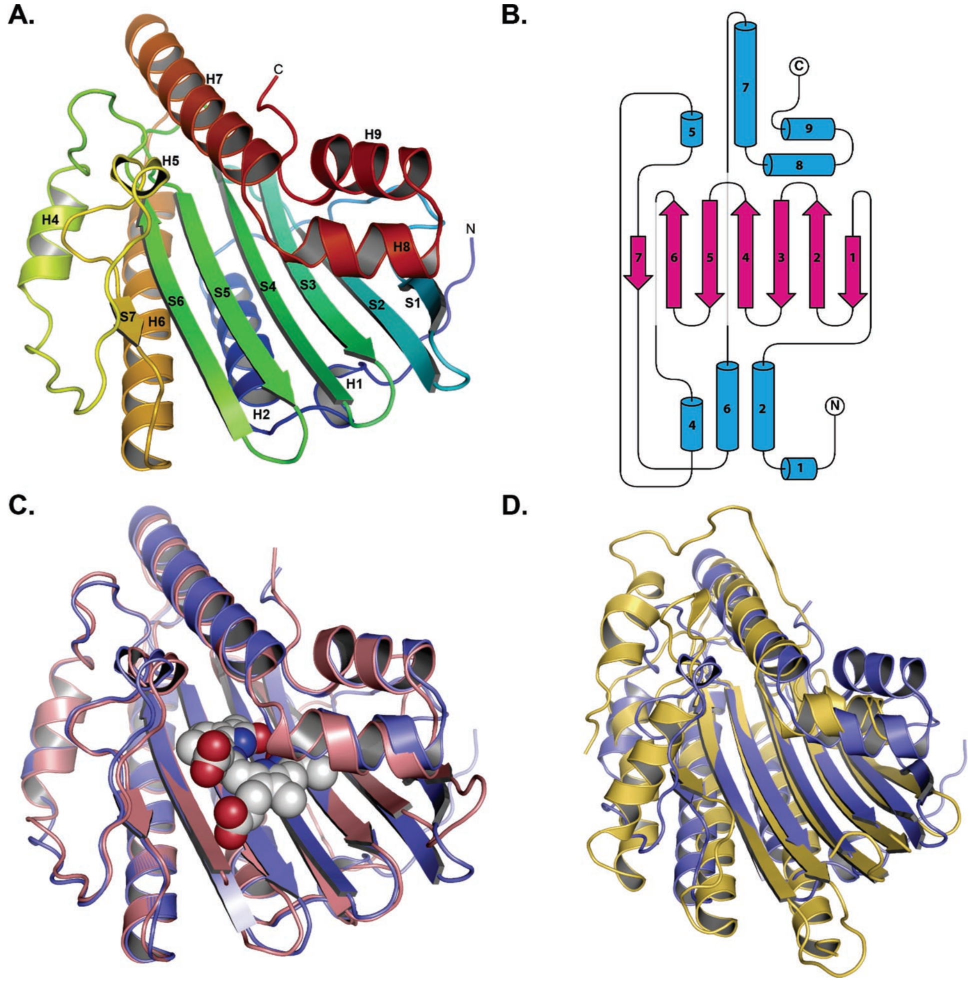

FIGURE 1: Comparative 3D structures of substrate-free *Nostoc* PcyA, BV-bound *Synechocystis* PcyA, and a hypothetical coproporphyrinogen III oxidase from *Leishmania major*. (A) Overall ribbon drawing of the *Nostoc* sp. PCC7120 crystal structure determined at 2.5 Å resolution in the absence of BV (pdb ID 2G18). The ribbon representation is rainbow-colored with the N-terminus colored in blue, ending with red at the C-terminus. (B) Topology schematic representation of the PcyA structure. Nomenclature of the secondary structure elements follows that of the recently determined *Synechocystis* sp. PCC6803 PcyA-biliverdin structure (*9*). The central β-sheet folds into a β-meander topology sandwiched between four helices both above and below. Helix H3, which consists of a single turn of the 3_{10}-helix in the *Synechocystis* structure, is not observed in the *Nostoc* structure. (C) Overlay of the *Synechocystis* PcyA-BV binary structure (salmon colored; pdb ID 2D1E) onto the apo *Nostoc* structure (slate blue color). The rmsd is 0.78 for 220 equivalent α-carbons. BV is drawn as CPK spheres with white carbon atoms. (D) Superposition of the *Nostoc* PcyA (slate blue) onto the putative coproporphyrinogen III oxidase from *Leishmania major* Lmaj006828 (yellow; pdb ID 1VJU). The rmsd between the two structures of 3.2 Å for 207 equivalent α-carbons only shares 11.9% sequence identity.

to confirm that the tentative holoprotein models were not grossly unstable. To identify candidate proton donors, Homolmapper was used with the sequence alignment (Figure S1, Supporting Information) to find residues conserved in $\geq$90% of each subfamily.

RESULTS AND DISCUSSION

PcyA Adopts a Single-Domain $\alpha/\beta/\alpha$ *Sandwich Fold that Is Similar to that of Coproporphyrinogen Oxidase.* The substrate-free *Nostoc* PcyA monomer adopts a globular single-domain fold with a seven-stranded antiparallel β-sheet sandwiched between four α-helices on each side (Figure 1A and B). Superposition of the structures of *Nostoc* PcyA (pdb code 2G18) and BV-bound PcyA (pdb code 2D1E), both from *Synechocystis* sp. PCC6803, indicates that the overall folds are nearly indistinguishable (Figure 1C). We will, therefore, adopt the secondary structure nomenclature for the *Synechocystis* enzyme in the following discussion (*9*). The topology of the central β-sheet of PcyA consists of a β-meander motif with helices H4 and H5 inserted between strands S6 and S7. Helices H5, H7, H8, and H9 all lie above the β-sheet (as depicted in Figure 1), whereas helices H1, H2, H4, and H6 lie below the β-sheet. In the *Synechocystis* PcyA structure, helix H3 forms one turn of a 3_{10}-helix between strands S4−S5, whereas the electron density of the *Nostoc* enzyme clearly defines a main-chain conformation in this region that falls outside the defined 3_{10}-helix torsion angles in all 12 monomers in the ASU. Consequently, helix H3 is not depicted in the *Nostoc* PcyA topology (Figure 1B).

Aside from the *Synechocystis* enzyme, the PDB database searches revealed that a hypothetical coproporphyrinogen III oxidase from *Leishmania major* Lmaj006828 (pdb code 1VJU) and yeast coproporphyrinogen III oxidase (pdb code 1TK1, 1TKL, and 1TLB (*28*)) have very similar topologies (Figure 1D). A DALI search resulted in a *Z* score of 15.5 (*29*) and a root mean square deviation (rmsd) of 3.2 Å for

207 equivalent α-carbons between *Nostoc* PcyA and *Leishmania* coproporphyrinogen III oxidase, which share only 12% sequence identity. Coproporphyrinogen III oxidase, a key enzyme in the heme biosynthetic pathway, catalyzes the oxygen-dependent decarboxylation of coproporphyrinogen III to yield protoporphyrinogen IX. Like PcyA, coproporphyrinogen III oxidase binds a tetrapyrrole substrate, and the proposed substrate-binding site of the latter (*28*) overlaps with that identified for PcyA (*9*). However, the two enzymes catalyze quite distinct reactions, one oxidative and the other reductive. The bilin substrate of PcyA also cannot adopt the fully cyclic configuration of coproporphyrinogen III. Therefore, the catalytic residues and mechanisms of the two enzymes are very different.

Comparison between Nostoc and Synechocystis PcyA Structures Reveals Substrate-Induced Structural Changes. A comparison of the substrate-free *Nostoc* PcyA structure with both *Synechocystis* PcyA structures reveals that the enzymes are very similar, as expected for enzymes with 59% sequence identity. The most pronounced differences seen between the two PcyAs lie in the loops between secondary structural elements and at the amino termini. The structural differences at the amino termini are likely to be the result of sequence divergence between the two species. The N-terminus of the *Synechocystis* enzyme is more hydrophobic and packs against a hydrophobic patch on the core of the protein (Figure S2A, Supporting Information). This interaction is seen for both the substrate-free and substrate-bound forms of the *Synechocystis* enzyme (*9*, *10*). In contrast, more polar amino acid substitutions found in the *Nostoc* enzyme contribute to the observed extension of the N-terminus away from the protein core and its interlocking interaction with a symmetry related N-terminal arm in an antiparallel β-strand handshake (Figure S2B, Supporting Information). This interaction is observed in 8 of the 12 monomers in the ASU, whereas in the other 4 monomers, the N-terminal arm is disordered. Other differences in the main-chain backbones of the *Nostoc* and *Synechocystis* enzymes occur around the rim of the BV binding pocket. Specifically, the S3−S4 and S5−S6 β-hairpin loops adopt different conformations, which are likely due to sequence variations, for example, Pro110 in *Synechocystis* PcyA, situated at the end of β-strand S5, is exchanged with Arg in the *Nostoc* enzyme, and Gly83, at the beginning of β-strand S4 in *Synechocystis* PcyA, is exchanged with Met in *Nostoc* PcyA.

Substrate-free *Nostoc* PcyA is more similar to the substrate-free *Synechocystis* enzyme (*10*) than the BV-bound *Synechocystis* enzyme (*9*). The superposition of all 12 *Nostoc* monomers in the ASU with the substrate-free and BV-bound *Synechocystis* structures gave rmsd ranges of 0.72−0.76 Å (229 equivalent α-carbons) and 0.78−0.86 Å (220 equivalent α-carbons), respectively. There are some significant structural differences between the two ligand-free enzyme structures near the BV binding pocket, the most significant one involving Arg149 and Glu150 (*Synechocystis* PcyA numbering). In the BV-bound *Synechocystis* enzyme (*9*), Arg149 ion pairs with the C-ring propionate side chain of the substrate (Figure 2A), whereas Glu150 points away from the binding pocket toward the solvent. In the substrate-free *Synechocystis* enzyme (*10*), these two residues flip orientations with Glu150 pointing toward the empty substrate-binding pocket and Arg149 flipping ∼180° into the solvent. In the ligand-free *Nostoc* structure, by contrast, both side-chains are positioned identically with the corresponding residues in the BV-bound *Synechocystis* structure in all 12 monomers within the ASU (Figure 2 and data not shown). Lys221 (in the H7−H8 loop that ion pairs with the BV B-ring propionate) adopts a solvent-exposed configuration in the ligand-free *Synechocystis* structure, whereas in the *Nostoc* structure, this lysine adopts a conformation similar to that of the *Synechocystis* BV-bound structure in all 12 monomers within the ASU (Figure 2A). These differences imply that the surface electrostatic potential (SEP) of ligand-free *Nostoc* PcyA is similar to that of ligand-bound *Synechocystis* PcyA rather than that of ligand-free *Synechocystis* PcyA. This argues against a critical role for SEP changes in recruiting ferredoxin only after BV binding, as had been recently proposed (*11*). It is nevertheless likely that both conserved positively charged residues are important to substrate binding.

To identify structural changes specific to substrate binding, we performed a comparison of the substrate-free *Nostoc* structure with the BV-bound *Synechocystis* structure. It is notable that these structures exhibit different orientations of the S1−S2 loop (Figure S3, Supporting Information). BV binding is likely to be the cause of this difference because BV-free *Synechocystis* PcyA also shows a S1−S2 loop conformation similar to that of the BV-free *Nostoc* enzyme. This conformational change appears to be triggered by the movement of Leu58 toward the BV D-ring as seen in the *Synechocystis* binary structure. This movement results in the shrinking of a cavity near the D-ring (Figure S3, Supporting Information), which could be functionally important, because the other end of this cavity is formed by Glu76, a residue implicated in proton transfer (see below). In the *Synechocystis* binary structure, this cavity is filled by the insertion of the Leu58 side chain to accommodate the binding of the D-ring exovinyl group. We hypothesize that this change in the size of the cavity will alter both the local dielectric constant and the pK_a of Glu76.

Another notable BV-induced change involves the loop between helices H7 and H8. Lying above BV as depicted in Figure 1, the H7−H8 loop contains residues that can hydrogen bond to the substrate. Asn219 points toward the solvent in the substrate-free *Nostoc* enzyme, whereas its amide side chain must move ∼6.5 Å upon BV binding to lie directly above the substrate in the bound structure (Figure 2A). In contrast, Asp220, whose carboxyl side chain is directed into the BV binding pocket in the apo structure, must swing out ∼9.2 Å in the binary structure to become solvent exposed (Figure 2A). Thr219 must also rotate ∼180° around χ_1 and shift 1.3 Å ($C_\alpha-C_\alpha$ distance) to accommodate the BV D-ring, where the $O_{\gamma1}$ is in hydrogen-bonding distance of the D-ring nitrogen. However, little movement of Lys221 is seen, which ion pairs to the BV propionate group (Figure 2A). The overall effect of these apparently BV-induced conformational changes is to create an extra helical turn at the N-terminal end of helix H8. This conformation is stabilized by the repositioning of the amide oxygen of Asn219, which forms a helical N-cap to H8, with Asn219 $O_{\delta1}$ hydrogen bonded to the main-chain nitrogen of Lys221. We believe that these conformational motions reflect BV binding rather than sequence variations because the structures of the substrate-free *Synechocystis* and *Nostoc*

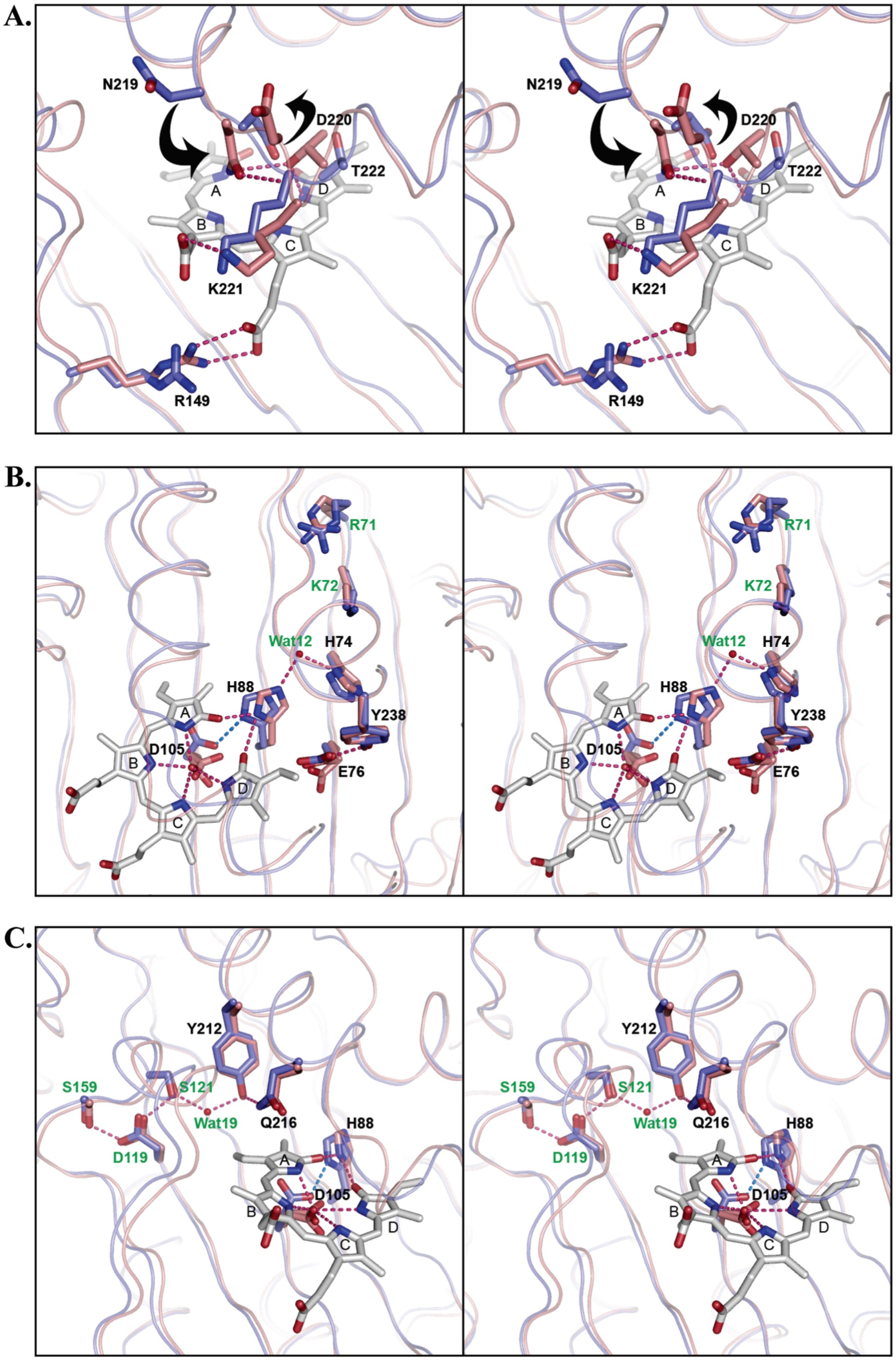

FIGURE 2: Comparative bilin-binding active sites of the *Nostoc* and *Synechocystis* PcyA enzymes. In all three panels, *Nostoc* PcyA is colored in slate blue, *Synechocystis* PcyA is colored in salmon, and BV substrate is shown as a stick model with white carbon atoms. Numbering corresponds to the *Synechocystis* enzyme. (A) Stereoview showing the differences observed for the H7−H8 loop. Black arrows illustrate the potential movement of residues upon binding BV. Predicted hydrogen bonds are drawn as dashed lines. (B) Stereoview showing the superposition of *Nostoc* and *Synechocystis* PcyA active sites and potential proton relay 1. In the *Nostoc* structure, His88 H-bonds with Asp105 (blue dashed line). In the BV-bound *Synechocystis* structure, Asp105 hydrogen bonds to the tetrapyrrole nitrogens, and His88 hydrogen bonds to BV O1 and O19 carbonyls and to bound Wat12. Wat12 lies near conserved Lys72, which is next to conserved Arg71, which is solvent exposed. The green-labeled residues could be involved in a proton relay to re-protonate His88 in the catalytic mechanism. Asp105 and Glu76 are observed in two conformations in the *Synechocystis* binary structure. (C) Stereoview showing residues near the A-ring vinyl group. Conserved residues involved in potential proton relay 2 are labeled green with hydrogen bonds drawn as dashed lines.

enzymes are nearly identical in the H7−H8 loop. Taken together, these analyses indicate that the H7−H8 loop folds down onto the BV substrate upon binding.

Structural Insights into the PcyA Catalytic Mechanism. A comparison of the substrate-bound and substrate-free structures demonstrates that the side-chains of putative catalytic residues reposition upon BV binding, including the critical His88 and Asp105 pair identified in previous studies (*8*). Interestingly, the 1.5 Å *Synechocystis* BV-bound PcyA structure revealed two side chain conformations for Asp105 (*9*). In the lower resolution substrate-free structures, only one conformation of Asp105 could be observed, with $N_{\delta 1}$ of His88 2.8 Å away from $O_{\delta 1}$ of Asp105 (Figure 2B). This implies that the side chains of His88 and Asp105 primarily

Table 2: Relative Activities of Nostoc PcyA Wild Type and Site-Directed Mutants[a]

proteins[b]	activity (% of wild-type)	products	remarks
PcyA	100	3*E*/3*Z*-PCB	ref 8
H85Q	5	3*E*/3*Z*-PCB	ref 8
H71Q	65	3*E*/3*Z*-PCB	ref 8
D102N	11	3*E*/3*Z*-PCB	ref 8
K218E	20	3*E*/3*Z*-PCB	ref 8
E73Q	20	3*E*/3*Z*-PΦB	this study

[a] Steady-state bilin reductase assays were performed as described previously (*8*). Integrated peak areas of 3*Z*/3*E*-PCB or 3*Z*/3*E*-PΦB reaction products from HPLC profiles were determined as a percentage of 3*Z*/3*E*-PCB of wild-type PcyA. [b] Nostoc PcyA numbering shown here.

exist as a carboxylate−imidazolium ion pair in the free enzyme. Upon BV binding, the two residues move apart, increasing their separation to 3.9 Å, and the side chain of Asp105 rotates ~70° about χ_1. The imidazole side chain of His88 repositions within H-bonding distance to one or both lactam carbonyl oxygens of the BV substrate ($N_{\delta 1}$ of H88 is 2.7 and 3.1 Å away from O1 and O19, respectively; Figure 2B). These data suggest that, upon substrate binding, the $N_{\delta 1}$ imidazolium proton of H88 transfers to the carboxylate side chain of Asp105, with subsequent formation of an equilibrium between two species: a major species with the neutral carboxylic acid H-bonded to both lactam oxygens and to the NH-group of the D-ring and a minor species consistent with an Asp105 carboxylate−BVH+ ion pair (*9*). In this scenario, neutral BV would formally bind to a charge−neutral binding pocket, followed by the formation of a small amount of BVH+ cation. Although it is not possible to ascertain the BV protonation site from the crystallographic data, we have argued that O-protonation on the D-ring lactam oxygen atom would be the likely proton acceptor on steric grounds (*8*). It is noteworthy that O-protonation of bilins occurs preferentially to N-protonation in bilins constrained to cyclic conformations (*30*), as is the case in the crystal structure of the BV−PcyA complex. Moreover, O-protonation of the BV substrate is consistent with the presence of a near-infrared (NIR) absorbing shoulder in the UV−visible spectrum of BV complexes of FDBRs (*6*, *7*). Thus, the crystallographic and biochemical data support the interpretation that the critical His88−Asp105 pair directly participates in substrate protonation.

The Glu76 carboxylic acid side chain also adopts two conformations upon BV binding (*9*). In both substrate-free structures (*10*), only one conformation is observed, closely resembling the higher occupancy species in the complex (Figure 2B). This conformation is hydrogen bonded to the phenolic side chain of Tyr238 and is also closely apposed to the D-ring exovinyl group in the bound structure. Glu76 is, therefore, well positioned to donate a proton to the bilin radical intermediate upon reduction (*9*). Other residues implicated in the catalytic mechanism (Table 2) do not appear to undergo significant conformational changes upon substrate binding (Figure 2B and C), including the essential Lys221 (Table 2 and ref 9 (*9*)). The presence of a bound water molecule (Wat12) in the BV-bound structure that lies between the His74 and His88 side chains (*9*) as well as the locations of fully conserved residues Lys72 and Arg71 suggests that these residues may form a proton shuttle from the bulk solvent to His88 (Figure 2B). Asp119 is located within a hydrogen-bonding network to the conserved Tyr212 and Gln216, both of which lie directly above the endovinyl group of BV (Figure 2C). Although Tyr212 and Glu216 are implicated in endovinyl reduction (*9*), Asp119 probably plays a more important role in overall protein folding rather than a specific catalytic function because of its general conservation in the FDBR family (Figure S1, Supporting Information). Finally, the location of Lys221 on the lip of the PcyA active site is well positioned for substrate binding via a salt link to the BV B-ring propionate (Figure 2A; (*9*)). The strongly positive surface potential near the substrate binding site is likely to represent the site of ferredoxin interaction with FDBRs during catalysis, as has been proposed (*9*, *10*).

E76Q Mutant Catalyzes A-Ring Endovinyl Reduction to Produce Phytochromobilin. In light of these structural insights, site-directed mutagenesis was undertaken to extend our prior analysis of K221E, H74Q, D105N, and H88Q mutants, all of which exhibit reduced steady-state turnover activity (Table 2; (*8*)). Because Glu76 appears to be in a good position to donate a proton to the D-ring vinyl group upon electron transfer (*9*), the *Nostoc* E73Q mutant (i.e., E76Q mutant in *Synechocystis* PcyA and described as E76Q hereafter) was expressed and biochemically analyzed. E76Q was able to metabolize BV, but, strikingly, the two-electron reduced product 3*Z*/3*E*-PΦB was obtained instead of the expected four-electron product 3*Z*/3*E*-PCB (Figure 3A). Because wild-type PcyA converts BV to PCB via the intermediate 18^1,18^2-DHBV (*6*), the E76Q mutation, thus, changed the double-bond reduction regiospecificity of PcyA to reduce only the A-ring endovinyl group. Optical measurements of the E73Q−BV complex also revealed the presence of the NIR absorbing species previously reported for wild-type PcyA (Figure 3B, top panel). Moreover, the addition of 1 to 10 equivs of NADPH to the E73Q−BV complex produced intermediates with a characteristic radical spectral signature (*7*), which appeared and decayed with kinetics similar to that of the wild-type enzyme (Figure 3B, bottom three panels). These results strongly suggest that the E73Q mutant still supports the O-protonation (via Asp105) of the bound BV substrate and proton-coupled electron transfer. However, the turnover efficiency and the 3*Z*/3*E*-PΦB product yields of this mutant are less than those of authentic phytochromobilin synthase HY2 (Figure 3A and data not shown), suggesting that additional mutations are required to convert PcyA into a physiologically competent PΦB synthase.

His88 Participates in Both D-Ring Exovinyl and A-Ring Endovinyl Reductions. Previous studies suggested that His88 functions as the secondary proton donor for D-ring exovinyl reduction (*8*). This interpretation is consistent with the crystal structure of BV-bound PcyA (*9*), which shows the imidazole ring of His88 within H-bonding distance of the O19 carbonyl oxygen (Figure 2B). Because His88 is also close to the O1-carbonyl oxygen, its imidazole side chain is also in good position to mediate proton transfer to the A-ring during endovinyl reduction. To test this hypothesis, we compared the reduction of the endovinyl group of the 18^1,18^2-DHBV intermediate by PcyA wild type and the H88Q (i.e., H85Q mutant in *Nostoc* PcyA) mutant under single-turnover assay conditions. As shown in Figure 4A, wild-type PcyA converts 18^1,18^2-DHBV to PCB via a series of spectrally distinct

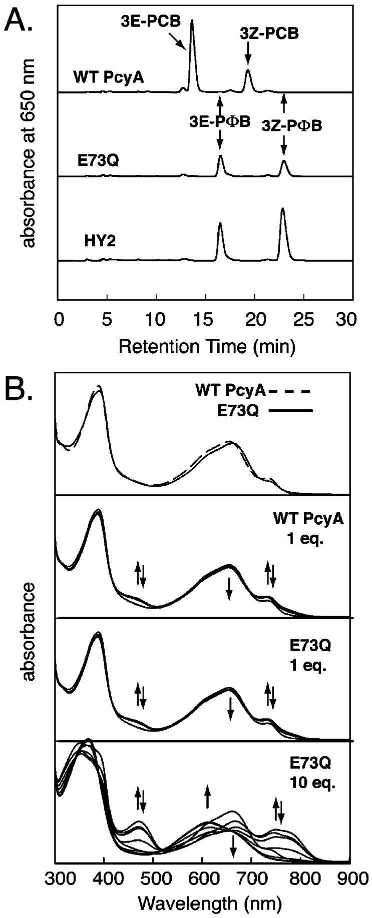

FIGURE 3: Biochemical analysis of the E76Q mutant (E73Q mutant of *Nostoc* PcyA). (A) Comparative product analysis of steady-state bilin reductase assays of wild-type *Nostoc* PcyA, *Nostoc* E73Q mutant, and *A. thaliana* HY2. Elution positions of 3*Z*-PCB, 3*E*-PCB, 3*Z*-PΦB, and 3*E*-PΦB are indicated by arrows (upper panel), and absorbance at 650 nm was monitored. (B) Spectral analysis of wild-type and E73Q mutant of *Nostoc* PcyA under single-turnover conditions. Absorption spectra of 10 μM PcyA−BV and E73Q−BV complexes are shown in the top panel. Time courses of BV reduction by wild-type PcyA and E73Q following the addition of 1 (middle two panels) and 10 electron (bottom panel) equivs of NADPH are shown (3 nM FNR, 10 μM Fd, and an oxygen scavenging system included (*7*)). Absorption spectra were monitored for 10 min; 1 min intervals are shown. The absorbance increases followed by decays at 470 and 770 nm in the bottom panel are indicated by double arrows, whereas absorbance decreases at 650 nm and increases at 600 nm are indicated by single arrows. The thick-lined curves represent spectra 60 min after the addition of the reductant.

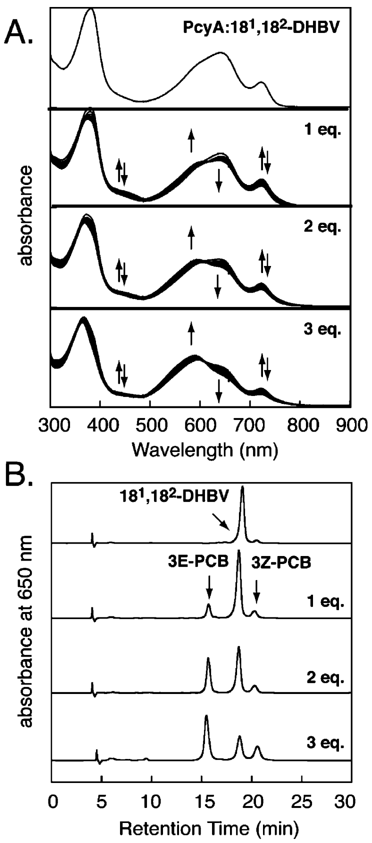

FIGURE 4: Catalytic conversion of 18^1,18^2-DHBV by *Nostoc* PcyA. (A) Absorption spectroscopy of the 18^1,18^2-DHBV reaction. The time course of BV reduction by *Nostoc* PcyA was monitored spectrophotometrically following the sequential addition of 1−3 electron equivs of NADPH to solutions of 10 μM PcyA−BV complex, 3 nM FNR, 10 μM Fd, and an oxygen scavenging system as described previously (*7*). Absorption spectra were monitored for 10 min; 1 min intervals are shown. Twenty minute periods were provided between subsequent additions of NADPH. Absorbance increases followed by decays at 460 and 770 nm are indicated by double arrows, whereas absorbance decreases at 650 nm and increases at 590 nm are indicated by single arrows. The thick-lined curves represent spectra 60 min after the addition of the reductant. (B) HPLC analysis of the *Nostoc* PcyA-mediated conversion of 18^1,18^2-DHBV to PCB. Reaction mixture aliquots (200 μL) corresponding to the spectra shown in Figure 4A were withdrawn, and the extracted bilin pigments were analyzed by reversed phase HPLC. Elution positions of 3*Z*-PCB, 3*E*-PCB, and the 18^1,18^2-DHBV standard are indicated by arrows, and the absorbance at 650 nm was monitored.

intermediates that are quite similar to those observed for the initial two-electron reduction of BV to 18^1,18^2-DHBV (*7*). HPLC analyses confirm that 3*Z*/3*E*-PCB is the catalytic product, although an excess of electron equivalents was needed to effect full conversion (Figure 4B). In contrast, the H88Q mutant was unable to support the conversion of 18^1,18^2-DHBV to PCB, even though this mutant formed a stable complex with 18^1,18^2-DHBV. Consistent with its lack of NIR absorbing species (Figure 5), previously assigned to the protonated bilin species for the 18^1,18^2-DHBV complex of wild-type PcyA (*7*, *8*), this result suggests that His88-dependent O-protonation is required for catalysis. Like the BV−H88Q enzyme complex (*8*), the addition of one electron equivalent of NADPH to the 18^1,18^2-DHBV−H88Q complex yielded stable, albeit small amounts of radical intermediates. Using a 5-fold molar excess of NADPH, 18^1,18^2-DHBV−H88Q could be fully converted to a stable radical complex (Figure 5, bottom). These results indicate that His88 not only participates in the exovinyl reduction, but also plays a central role in the reduction of the endovinyl group in the overall PcyA-mediated conversion of BV to PCB.

Revised Mechanism of PcyA-Mediated BV Reduction. On the basis of the three PcyA crystal structures and biochemical analyses of the *Nostoc* enzyme, we propose a mechanism for PcyA-mediated BV reduction, which is depicted in Figure 6. Similar to the proposal of Hagiwara and colleagues (*9*), we suggest that the carboxylic acid groups of Asp105 and Glu76 serve as proton donors for D-ring exovinyl reduction. We further hypothesize that BV binding alters the relative p*K*a values of the His88 imidazole and Asp105 carboxylic acid side chains to favor the neutral complex. Following proton transfer from Asp105 (D_0) to the O19 carbonyl

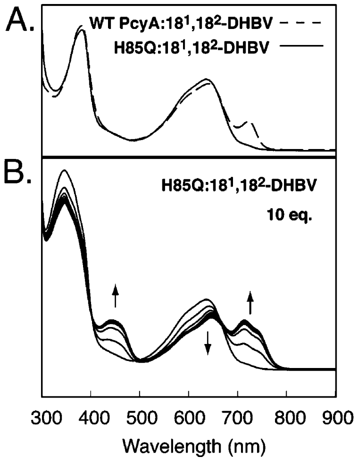

FIGURE 5: Metabolism of $18^1,18^2$-DHBV by the H88Q mutant (H85Q mutant of *Nostoc* PcyA). (A) Absorption spectra of solutions of 40 μM BV complexes of the wild type and H85Q mutant of *Nostoc* PcyA prior to the addition of the reductant. (B) Time courses of $18^1,18^2$-DHBV reduction, monitored spectrophotometrically for 10 min at 1 min intervals after the addition of 10 electron equivs of reductant (i.e., 200 μM NADPH) to samples containing 40 μM preformed H85Q−$18^1,18^2$-DHBV complexes. Absorbance increases at 470 and 770 nm and decreases at 650 nm are indicated by single arrows. The peak around 340 nm overlapped with the blue absorption of BV corresponds to NADPH absorption.

oxygen, the neutral BV (bound) species equilibrates with the protonated BVH+ (cation) species. We envisage that the minor enzyme-bound BVH+ cation is the species that accepts the initial electron from reduced ferredoxin to yield the neutral radical species BVH•. This species is rapidly converted to the cation radical species BVH_2•+ by protonation of the O1-carbonyl oxygen. This interconversion utilizes proton relay 1, consisting of Arg71 and Lys72, that is well positioned to shuttle a proton from the bulk solvent to re-protonate His88. Upon an electron transfer from a second reduced ferredoxin, $C18^2$-protonation of the exovinyl group by the Glu76 carboxylic acid side chain (D_1) would follow to produce the cationic intermediate 18^2-MHBVH+. Because this interconversion is not possible for the E76Q mutant, the alternative proton transfer to the C2-position of the A-ring could account for the distinct regiospecificity of this mutant (see below). Faster proton transfer to the exovinyl group rather than the alternative presumably accounts for the observed regiospecificity of the wild-type enzyme. Moreover, we envisage that the resulting Glu76−carboxylate anion is stabilized by H-bonding with nearby Tyr238 or by the formation of an ion pair with the imidazolium group of His74 (whose protonation via proton relay 1 is depicted in Figure 6). The generation of the fully reduced intermediate $18^1,18^2$-DHBVH$^+$ entails tautomerization of the O19 proton (D_2) to the 18^1-position.

We propose that endovinyl reduction occurs via a similar mechanism, with protonated His88 and possibly bound water (Wat19) representing the two catalytic proton donors. Upon ferredoxin-mediated electron transfer to DHBVH+, the reprotonated form of His88 (via proton relay 1) is well positioned to donate a proton to the O1 carbonyl of the DHBVH• neutral radical species (Figure 6). Following the fourth and final electron transfer to the protonated radical species $DHBVH_2$+•, we propose that the lactim proton on O1 (D_3) tautomerizes to the C2-position to produce the neutral trihydrobiliverdin lactam, $2,18^1,18^2$-THBVH. In this regard, His88H+ is well positioned to mediate the transfer of the O1 proton to produce the *R*-stereochemistry at C2. Moreover, the O1 proton is also likely to interact with the carboxylate side chain of Asp105, again favoring formation of the correct *R* stereoisomer at C2. Product release requires protonation of the $C3^2$-position, a process that could occur from the bulk solvent upon release or via proton donation from bound Wat19. In this regard, the Asp105 carboxylate might serve as a catalytic base to drive this interconversion as shown in Figure 6. It is also conceivable that the Asp119 carboxylic acid side chain could pivot close to the substrate to donate a proton to the nascent $C3^2$ anion (Figure 2C). Additional experimental work is needed to distinguish between the potential D_4 proton donors, (bulk water, Wat19, and/or Asp119). In view of the mixture of 3*E* and 3*Z* isomers of PCB obtained, we favor the protonation upon release into the bulk solvent. Finally, we envisage that product release is promoted by the loss of protein−bilin interactions (i.e., loss of H88−O1, E76−exovinyl, and Wat19−endovinyl interactions) as well as by the increase of catalysis-dependent unfavorable interactions (e.g., increased negative charge density in the bilin binding pocket and unfavorable van der Waals interactions between the polar residues juxtaposed near the newly reduced ethyl side chain).

Although much work remains to test the individual steps of this hypothetical mechanism, most of the available biochemical and structural data are consistent with this model. The guiding principles of this mechanism are as follows: intermolecular heteroatom (O- or N-) proton-transfer proceeds considerably faster than proton transfer to/from carbon (*31*), the proton shared by O19, O1 and Asp105 remains in place throughout the entire catalytic cycle, and product release is the rate-limiting step for catalysis under saturating levels of reduced ferredoxin. These assumptions will also be tested in future investigations.

Mechanistic Predictions for Other Members of the FDBR Family. Homology models have been proposed for the two-electron FDBRs HY2, PebA, and PebB, demonstrating a conserved positive surface potential region that could serve as the docking site for reduced ferredoxin (*9*). However, this previous study did not address the potential catalytic residues that might mediate each enzyme's specific catalytic conversion. To predict potential proton-donating residues for the other FDBRs, we examined the homology within each subfamily using new homology models, the FDBR sequences (Figure S1, Supporting Information), and Homolmapper (available from http://www.mcb.ucdavis.edu/faculty-labs/lagarias). This analysis demonstrates that each of the four classes of FDBRs have distinct groups of potential proton donors (Figure S4 and Table S1, Supporting Information), suggesting that FDBR regiospecificity is determined by the locations of proton donors.

These homology models allow us to propose residues in HY2, PebA, and PebB that are critical for their divergent regiospecificities. The plant PΦB synthase HY2 must donate protons to C2 and $C3^2$ to effect the conversion of BV to PΦB. HY2 exhibits a unique, conserved Cys131 residue that is well positioned for donation to $C3^2$ (Figure S4, top (Supporting Information)). This residue may account for the strict regiospecificity of native oat PΦB synthase (*32*), although recombinant HY2 yields a mixture of 3*E* and 3*Z* isomers of PΦB in our hands (Figure 3A). Proton transfer

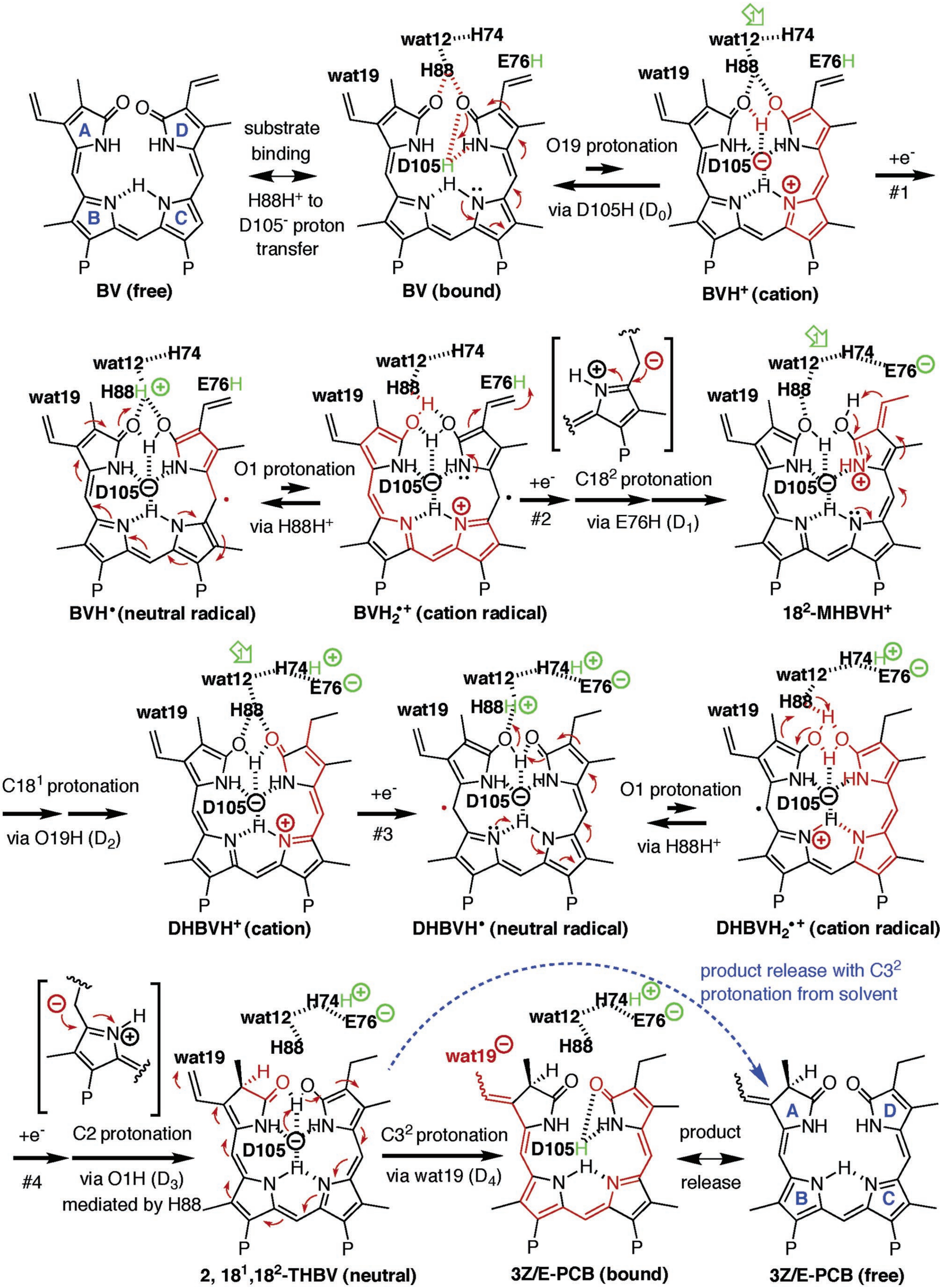

FIGURE 6: Proposed reaction mechanism of PcyA on the basis of crystal structures and biochemical analysis. PcyA catalyzes the complete overall four-electron reduction of BV to PCB. P stands for the propionate group. D_n represents proton donor n transfer. Residues near the bilin substrate/intermediates are written in bold. Red reflects the chemistry of each interconversion. Green reflects proton transfers within the protein. Proton relay 1 is indicated with a green arrow. The blue dashed arrow indicates product release with protonation from the bulk solvent. See text for details.

to C2 is likely to proceed via initial protonation of BV O1, possibly by Lys255, followed by isomerization to the C2 position. Interestingly, the initial holoprotein model of PebA does not place the reactive C15−C16 bond in close proximity to candidate proton donors (Figure S4, middle (Supporting Information)), other than Asp84 (equivalent to Asp105 in PcyA). All other potential proton donors lie close to the A ring instead. We, therefore, propose that PebA binds BV in the opposite orientation to PcyA (equivalent to rotation by ~180° about the pseudosymmetric C_2 axis at C10), placing these residues in proximity to the C15−C16 bond. Potential proton donors for this model are Tyr197 (equivalent to the possible D_4 Tyr212 in PcyA), Asp84, and Asp137. The initial PebB model places the bilin substrate in a good orientation for catalysis, with Asp100, Tyr216, and Lys223 as potential proton donors (Figure S4, bottom (Supporting Information)). It, therefore, seems likely that PebA and PebB have been retained as distinct enzymes through evolution because of the need to bind the substrate in opposite orientations. We anticipate that future work on FDBR regiospecificity will test these hypotheses.

ACKNOWLEDGMENT

We thank Wesley Sughrue for the construction of the E73Q mutant and critical review of the manuscript, Lixia Shang for assistance in bilin preparation, and Professor Dr. Bernhard Krautler for helpful discussions.

SUPPORTING INFORMATION AVAILABLE

Four Figures and one Table as described in the text. This material is available free of charge via the Internet at http://pubs.acs.org.

REFERENCES

1. Frankenberg, N. F., and Lagarias, J. C. (2003) Biosynthesis and Biological Function of Bilins, in *The Porphyrin Handbook. Chlorophylls and Bilins: Biosynthesis Structure and Degradation* (Guilard, R., Ed.) pp 211−235, Academic Press, New York.
2. Rockwell, N. C., Su, Y. S., and Lagarias, J. C. (2006) Phytochrome structure and signaling mechanisms, *Annu. Rev. Plant Biol. 57*, 837−858.
3. Glazer, A. N. (1999) Phycobiliproteins, in *Chemicals from Microalgae* (Cohen, Z., Ed.) pp 261−280, Taylor and Francis, London, England.
4. Ortiz de Montellano, P. R., and Auclair, K. (2003) Heme Oxygenase Structure and Mechanism, in *The Porphyrin Handbook. The Iron and Cobalt Pigments: Biosynthesis, Structure and Degradation*. (Guilard, R., Ed.) pp 183−210, Academic Press, New York.
5. Frankenberg, N., Mukougawa, K., Kohchi, T., and Lagarias, J. C. (2001) Functional genomic analysis of the HY2 family of ferredoxin-dependent bilin reductases from oxygenic photosynthetic organisms, *Plant Cell 13*, 965−978.
6. Frankenberg, N., and Lagarias, J. C. (2003) Phycocyanobilin: ferredoxin oxidoreductase of Anabaena sp. PCC 7120. Biochemical and spectroscopic characterization, *J. Biol. Chem. 278*, 9219−9226.
7. Tu, S., Gunn, A., Toney, M. D., Britt, R. D., and Lagarias, J. C. (2004) Biliverdin reduction by cyanobacterial phycocyanobilin: ferredoxin oxidoreductase (PcyA) proceeds via linear tetrapyrrole radical intermediates, *J. Am. Chem. Soc. 126*, 8682−8693.
8. Tu, S., Sughrue, W., Britt, R. D., and Lagarias, J. C. (2006) A Conserved histidine-aspartate pair is required for exovinyl reduction of biliverdin by a cyanobacterial phycocyanobilin:ferredoxin oxidoreductase, *J. Biol. Chem. 281*, 3127−3136.
9. Hagiwara, Y., Sugishima, M., Takahashi, Y., and Fukuyama, K. (2006) Crystal structure of phycocyanobilin:ferredoxin oxidoreductase in complex with biliverdin IXα, a key enzyme in the biosynthesis of phycocyanobilin, *Proc. Natl. Acad. Sci. U.S.A. 103*, 27−32.
10. Hagiwara, Y., Sugishima, M., Takahashi, Y., and Fukuyama, K. (2006) Induced-fitting and electrostatic potential change of PcyA upon substrate binding demonstrated by the crystal structure of the substrate-free form, *FEBS Lett. 580*, 3823−3828.
11. Doublié, S. (1997) Preparation of Selenomethionyl Proteins for Phase Determination, in *Methods in Enzymology* (Carter, J. C. W., and Sweet, R. M., Eds.) pp 523−530, Academic Press, New York.
12. Hendrickson, W. A., Horton, J. R., and LeMaster, D. M. (1990) Selenomethionyl proteins produced for analysis by multiwavelength anomalous diffraction (MAD): a vehicle for direct determination of three-dimensional structure, *EMBO J. 9*, 1665−1672.
13. Otwinowski, Z., and Minor, W. (1997) Processing of X-ray Diffraction Data Collected in Oscillation Mode, in *Methods in Enzymology* (C. W. Carter, J., and Sweet, R. M., Eds.) pp 307−326, Academic Press, New York.
14. Matthews, B. W. (1968) Solvent content of protein crystals, *J. Mol. Biol. 33*, 491−497.
15. Terwilliger, T. C., and Berendzen, J. (1999) Automated structure solution for MIR and MAD, *Acta Crystallogr., Sect. D 55*, 849−861.
16. Terwilliger, T. C. (1999) Reciprocal-space solvent flattening, *Acta Crystallogr., Sect. D 55*, 1863−1871.
17. Terwilliger, T. C. (2000) Maximum likelihood density modification, *Acta Crystallogr., Sect. D 56*, 965−972.
18. Cowtan, K. (1994) DM: An automated procedure for phase improvement by density modification. Joint CCP4 and ESF-EACBM Newsletter on Protein, *Crystallography 31*, 34−38.
19. McCoy, A. J., Grosse-Kunstleve, R. W., Storoni, L. C., and Read, R. J. (2005) Likelihood-enhanced fast translation functions, *Acta Crystallogr., Sect. D 61*, 458−464.
20. Emsley, P., and Cowtan, K. (2004) Coot: model-building tools for molecular graphics, *Acta Crystallogr., Sect. D 60*, 2126−2132.
21. Murshudov, G. N., Vagin, A. A., and Dodson, E. J. (1997) Refinement of macromolecular structures by the maximum-likelihood method, *Acta Crystallogr., Sect. D 53*, 240−255.
22. Laskowski, R. A., Macarthur, M. W., Moss, D. S., and Thornton, J. M. (1993) Procheck - a Program to check the stereochemical quality of protein structures, *J. Appl. Crystallogr. 26*, 283−291.
23. Ramakrishnan, C., and Ramachandran, G. N. (1965) Stereochemical criteria for polypeptide and protein chain conformations. II. Allowed conformations for a pair of peptide units, *Biophys. J. 5*, 909−933.
24. Fiser, A., and Sali, A. (2003) Modeller: generation and refinement of homology-based protein structure models, *Methods Enzymol. 374*, 461−491.
25. Humphrey, W., Dalke, A., and Schulten, K. (1996) VMD: visual molecular dynamics, *J. Mol. Graphics 14*, 33−38.
26. Lindahl, E., Hess, B., and van der Spoel, D. (2001) GROMACS 3.0: A package for molecular simulation and trajectory analysis, *J. Mol. Model. 7*, 306−317.
27. Fischer, A. J., Rockwell, N. C., Jang, A. Y., Ernst, L. A., Waggoner, A. S., Duan, Y., Lei, H., and Lagarias, J. C. (2005) Multiple roles of a conserved GAF domain tyrosine residue in cyanobacterial and plant phytochromes, *Biochemistry 44*, 15203−15215.
28. Phillips, J. D., Whitby, F. G., Warby, C. A., Labbe, P., Yang, C., Pflugrath, J. W., Ferrara, J. D., Robinson, H., Kushner, J. P., and Hill, C. P. (2004) Crystal structure of the oxygen-dependant coproporphyrinogen oxidase (Hem13p) of Saccharomyces cerevisiae, *J. Biol. Chem. 279*, 38960−38968.
29. Holm, L., and Sander, C. (1993) Protein structure comparison by alignment of distance matrices, *J. Mol. Biol. 233*, 123−138.
30. Krois, D. (1991) Geometry versus basicity of bilatrienes—stretched and helical protonated biliverdins, *Monatsh. Chem. 122*, 495−506.
31. Kresge, A. J. (1975) What makes proton-transfer fast, *Acc. Chem. Res. 8*, 354−360.
32. McDowell, M. T., and Lagarias, J. C. (2001) Purification and biochemical properties of phytochromobilin synthase from etiolated oat seedlings, *Plant Physiol. 126*, 1546−1554.

BI062038F